Understanding the Reduction Behavior of VO_x/CeO_2 on a Molecular Level: Combining Temperature-Programmed Reduction with Multiple In Situ Spectroscopies and X-Ray Diffraction

Leon Schumacher[a], Marc Ziemba[a], Kai Brunnengräber[b], Lea Totzauer[c], Kathrin Hofmann[c], Bastian J.M. Etzold[b], Barbara Albert[c], Christian Hess[a]*

[a]Technical University of Darmstadt, Department of Chemistry, Eduard-Zintl-Institut für Anorganische und Physikalische Chemie, Alarich-Weiss-Str. 8, 64287 Darmstadt, Germany.

[b]Technical University of Darmstadt, Department of Chemistry, Ernst-Berl-Insitut für Technische und Makromolekulare Chemie, Alarich-Weiss-Str. 8, 64287 Darmstadt, Germany.

[c]Technical University of Darmstadt, Department of Chemistry, Eduard-Zintl-Institut für Anorganische und Physikalische Chemie, Alarich-Weiss-Str. 12, 64287 Darmstadt, Germany.

*Corresponding Author (E-Mail: christian.hess@tu-darmstadt.de)

TOC

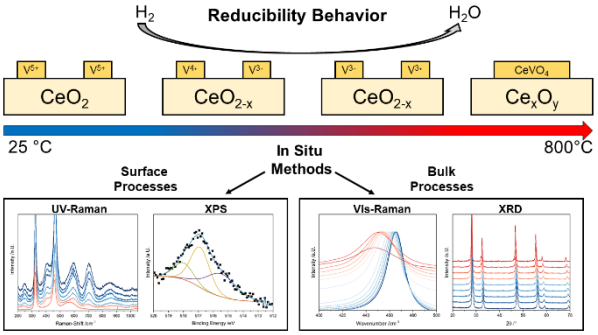
H2
Reducibility Behavior
H2O
V5+
V5+
CeO2
V4+
V3+
CeO2-x
V3+
V3+
CeO2-x
CeVO4
CexOy
25 °C
800°C
In Situ
Methods
Surface
Processes
Bulk
Processes
UV-Raman
XPS
Vis-Raman
XRD

Abstract

As catalytic processes become more important in academic and industrial applications, an intimate understanding is highly desirable to improve their efficiency on a rational basis. Since thorough mechanistic investigations require an elaborate and expensive spectroscopic and theoretical analysis, it is a major goal to link mechanistic insights to simple descriptors, such as the reducibility, that are accessible by temperature-programmed reduction (TPR) experiments, to bridge the gap between fundamental understanding and application of catalysts. In this work, we present a detailed in situ spectroscopic analysis of TPR results from loading-dependent VO_x/CeO_2 catalysts, using in situ multi-wavelength Raman, IR, UV-Vis, and quasi in situ X-ray photoelectron spectroscopy, as well as in situ X-ray diffraction. The catalyst reduction shows a complex network of different processes, contributing to the overall reducibility, which are controlled by the unique interaction at the vanadia-ceria interface. The temperatures at which they occur depend significantly on the nuclearity of the surface vanadia species. By elucidating the temperature- and vanadia loading-dependent behavior we provide a fundamental understanding of the underlying molecular processes, thus developing an important basis for interpretation of the reduction behavior of other oxide catalysts.

Introduction

Catalytic processes are a significant part of both the chemical industry and academic research, whereby the choice of the catalyst material is of great importance to the overall process performance. For many applications, supported materials are the best option due to their high activity, stability and separability[1] but the choice of the support is crucial, as different supports can change the catalytic activity significantly.[2–4] A commonly used support in oxidation reactions is ceria, due to its outstanding redox properties. These are often attributed to ceria's ability to form oxygen vacancies, where a lattice oxygen atom is consumed in the reaction and an oxygen vacancy is created along with two Ce^{3+} ions. The latter can then be regenerated using either oxygen from the gas-phase or subsurface oxygen, which is transported to the surface by diffusion.[5,6] Therefore, due to its redox properties, ceria is an excellent support material and has been employed in a variety of reactions, such as NO_2 storage,[7] NH_3 selective catalytic reduction (SCR),[8] CO oxidation,[9] reverse water-gas shift reaction,[10] and CO_2 hydrogenation,[11] as well as alcohol[12] and alkane[13] oxidative dehydrogenations (ODHs). The corresponding active phases are very diverse and can typically be either a metal (e.g. gold,[10] copper,[14] platinum,[15]) or an oxide (e.g. MnO_x,[16] VO_x,[13] MoO_x,[17]), depending on the application.

A catalyst commonly used in the oxidation of alcohols and short chain alkanes is ceria-supported vanadia (VO_x/CeO_2).[12,13,18] The reducibility of CeO_2 in this system is often cited as the reason for the good catalytic performance in oxidation reactions and is accessible by H_2 temperature-programmed reduction (TPR) measurements. However, a detailed understanding of the catalyst reduction on a molecular level through spectroscopic means is still lacking.[3,19–23] Furthermore, the intimate interaction between vanadia and ceria has a significant influence on the reduction behavior of the catalyst as it has often been described in the literature that ceria keeps vanadia in its highest oxidation state and vanadia interacts with lattice oxygen as well as oxygen vacancies on the surface.[18,22,24–27] Therefore, the reduction behavior is much more complicated and cannot be fully understood by using TPR only. It would therefore be highly desirable to link the measured TPR data to a molecular understanding of the reduction process, as obtained by spectroscopy, so that the easily available descriptor, the reducibility, could be used for the rational enhancement of catalytic structure and performance. While previous studies have started to explain some aspects of TPR by spectroscopy[28,29] and on ceria during hydrogen treatment[20,22,30], there have been no

reports in the literature that address VO_x/CeO_2 catalysts at different vanadia loadings, although the loading heavily influences the materials` properties, or with multiple supplementary in situ spectroscopies to cover the TPRs full temperature range.

TPR has been used to characterize catalysts in more applied technical studies (e.g. for VO_x/TiO_2 systems[31]), thus allowing to bridge the gap between detailed molecular investigations by spectroscopy and technical investigations used for catalyst optimization, thereby increasing the amount of knowledge obtainable by measurements, which can be performed with comparable ease. Although technical catalysts have a much more complex composition than their academically used counterparts, there are still based on the properties of the main active part, which are then modified by additional elements. Therefore, understanding the fundamental properties of the main component is of great importance for its further optimization.

In this study, we aim at a fundamental understanding of the reduction behavior of VO_x/CeO_2 catalysts with three different vanadium loadings below vanadia crystal formation to deepen the understanding of ceria's properties in oxidation catalysis as well as the interplay between the ceria support and its active phase. We apply multiple in situ methods, including multi-wavelength Raman, UV-Vis, DRIFTS, and XRD to explain on a molecular level the TPR results obtained over a wide range of temperatures and to gain detailed insight into the catalysts` behavior under reducing conditions. Our approach can readily be transferred to other catalytically relevant materials, such as VO_x/TiO_2 catalysts, to explain their reducibility behavior in a comprehensive manner. Furthermore, other methods, such as temperature-programmed oxidation (TPO) and temperature-programmed desorption (TPD) might also be explained in detail in the future by applying similar approaches.

Experimental Section

Catalyst Preparation. The ceria support was prepared as previously described[6] and loaded with vanadia by incipient wetness impregnation. Three different loadings were prepared by mixing 1 g of ceria with 0.5 mL of differently concentrated precursor solutions (1.07 mol/L, 0.51 mol/L, and 0.21 mol/L) containing vanadium(V) oxytriisopropoxide (≥97%, Sigma Aldrich) and 2-propanol (99.5%, Sigma Aldrich). The samples were then heated to 600 °C at a heating rate of 1.5 °C/min and calcined for 12 h. The specific surface was determined by analysis of the nitrogen adsorption and desorption isotherms recorded on a Surfer analyzer (Thermo Fisher) after drying the samples in a vacuum for 24 h. The isotherms were then analyzed by multipoint Brunauer–Emmett–Teller (BET) analysis and the specific surface area was determined to be 61.4 m²/g, yielding vanadium loadings of 2.83 V/nm² (2.32 wt% V_2O_5), 1.36 V/nm² (1.11 wt% V_2O_5), and 0.57 V/nm² (0.47 wt% V_2O_5). Higher vanadium loadings were not considered since vanadia crystallites were shown to be present at loadings >2.9 V/nm².[32] The resulting catalyst powders were subsequently pressed at a pressure of 2000 kg/m² for 20 s, ground and then sieved using a combination of sieves to obtain 200-300 µm sized particles.

Reduction Procedure. The catalyst sample was placed in the reaction chamber (see below) and was dehydrated at 365 °C in 12.5% O_2/He for 1 h. After the samples had cooled to room temperature, the gas-phase was switched to 7% H_2/Ar (total flow rate: 40 mL_n/min). The temperature was increased stepwise to 550 °C using 45 °C steps and a spectrum was recorded at each temperature. This procedure was performed for all methods except for quasi in situ XPS, DRIFTS, in situ XRD, and TPR, which will be described separately in the corresponding sections.

Temperature Programmed Reduction (TPR). TPR was performed on a Micromeritics 3Flex instrument. The sample was loaded in a quartz reactor and pre-treated by oxidation in synthetic air (20% O_2 in N_2, Westfalen) at 400 °C for 1 h, with a flowrate of 50 mL_n/min. The sample was then cooled down to 40 °C, while being flushed with 50 mL_n/min argon. After cooling down, the gas was switched to 50 mL_n/min 7% H_2/Ar. After waiting for 1.5 h for the reactor and instrument to be fully purged, TPR was performed by heating the sample up to 850 °C with a heating rate of 5 K/min. Consumption of hydrogen was detected using a thermal conductivity detector (TCD). During the measurement, a cold trap cooled to –10 °C was placed between the sensor

and the sample. To confirm the accuracy of the temperature calibration, V_2O_5 was measured as a well-known reference sample (see Figure S1).[33] To integrate the TCD signal, a baseline correction was performed, taking the three minima before and after the first hydrogen consumption region as well as before the phase-transition region as anchor points.

UV-Raman Spectroscopy. UV-Raman spectroscopy was performed at an excitation wavelength of 385 nm generated by a laser system based on a Ti:Sa solid state laser pumped by a frequency-doubled Nd:YAG laser (Coherent, Indigo). The fundamental wavelength is frequency doubled to 385 nm using a LiB_3O_5 crystal. The light is focused onto the sample, and the scattered light is collected by a confocal mirror setup and focused into a triple stage spectrometer (Princeton Instruments, TriVista 555), as described previously.[32] Finally, the Raman contribution is detected by a charge-coupled device (CCD, 2048×512 pixels) cooled to –120 °C. The spectral resolution of the spectrometer is 1 cm^{-1}. For Raman experiments, 70 mg of sample was placed in a CCR 1000 reactor (Linkam Scientific Instruments) equipped with a CaF_2 window (Korth Kristalle GmbH). A fluidized bed reactor was employed to avoid laser-induced damage, allowing the use of a laser power of 9 mW at the location of the sample. Data processing included cosmic ray removal and background subtraction.

Visible Raman Spectroscopy. Visible (Vis)-Raman spectroscopy was performed at 514 nm excitation, emitted from an argon ion gas laser (Melles Griot). The light was focused onto the sample, gathered by an optical fiber and dispersed by a transmission spectrometer (Kaiser Optical, HL5R). The dispersed Raman radiation was subsequently detected by an electronically cooled CCD detector (–40 °C, 1024×256 pixels). The spectral resolution was 5 cm^{-1} with a wavelength stability of better than 0.5 cm^{-1}. For Raman experiments, 70 mg of catalyst was filled into a CCR 1000 reactor (Linkam Scientific Instruments), equipped with a quartz window (Linkam Scientific Instruments). A fluidized bed reactor was employed to avoid laser-induced damage, allowing the use of a laser power of 6 mW at the location of the sample. Data analysis of the Raman spectra included cosmic ray removal and an auto new dark correction. The F_{2g} mode was fitted using one Lorentzian function without any positional restriction due to the possible occurrence of red-shifts.[34]

Diffuse Reflectance UV-Vis Spectroscopy. Diffuse reflectance (DR) UV-Vis spectra were recorded on a Jasco V-770 UV-Vis spectrometer. Dehydrated $BaSO_4$ was used

as the white standard. For each experiment, 90 mg of catalyst was put in the commercially available reaction cell (Praying Mantis High Temperature Reaction Chamber, Harrick Scientific) equipped with transparent quartz glass windows.

X-ray Photoelectron Spectroscopy (XPS). XP spectra were recorded on a modified LHS/SPECS EA200 MCD system described previously.[35–37] The XPS system was equipped with a Mg Kα source (1253.6 eV, 168 W), and the calibration of the binding energy scale was performed with Au $4f_{7/2}$ = 84.0 eV and Cu $2p_{3/2}$ = 932.67 eV signals from foil samples. The samples were treated in 12.5% O_2/Ar for 1 h before the measurements and with 7.5% H_2/Ar for 30 minutes after the measurements, both at 300 °C at a total flow rate of 40 mL/min.

The subsequent transfer of the sample to the analysis chamber was performed without exposure to air (quasi in situ). Sample charging was taken into account by setting the u''' peak of the Ce 3d signal to 916.7 eV.[38] Detailed spectra were recorded at a resolution of 0.1 eV. The X-ray satellite peaks due to the use of a non-monochromatic source were subtracted from the spectra. The deconvolution of the spectra was performed analogously for all measurements using Gauss–Lorentzian product functions (30/70), whereby the background was subtracted by the Shirley method.

V:Ce and O:Ce ratios were obtained from a least-squares fit analysis by integrating the Ce 3d signal and the O 1s or the V $2p_{3/2}$ signal after a Shirley background subtraction from the detailed spectra and by applying the same integration boundaries. The resulting areas were corrected with the corresponding relative sensitivity factors, i.e., 10 for the Ce 3d, 0.66 for the O 1s and 1.3 for the V $2p_{3/2}$ signal.[39]

Diffuse Reflectance Infrared Fourier Transform Spectroscopy (DRIFTS). DRIFT spectra were recorded on a Vertex 70 spectrometer (Bruker), equipped with a liquid nitrogen–cooled mercury cadmium telluride (MCT) detector, operating at a resolution of 1 cm^{-1}. Dehydrated potassium bromide was employed as an infrared transparent sample for the background spectrum. For each experiment, 90 mg of the catalyst was placed in the reaction cell (Praying Mantis High Temperature Reaction Chamber, Harrick Scientific) equipped with transparent KBr windows.

The sample was dehydrated at 365 °C in 12.5% O_2/He for 1 h, subsequently heated in 7% H_2/Ar to 550 °C and kept at 550 °C for 30 minutes until a steady state was reached. After the gas-phase had been switched to pure He, the sample was rapidly cooled down to room temperature (approx. 1 min) and a spectrum was recorded.

Data processing consisted of background removal by subtraction of a baseline formed by 12 anchor points. A background spectrum of the gas-phase was recorded using KBr as an infrared-transparent sample. The propane gas-phase and the operando spectra were then normalized to the propane gas-phase peak at ~3000 cm^{-1} and subtracted to remove propane gas-phase contributions.

X-ray Diffraction (XRD). X-Ray diffraction patterns were recorded on an Empyrean system (Malvern Panalytical) in Bragg–Brentano geometry using CuK_α radiation and a PIXcel^{1D} detector. For in situ analysis, 90 mg of catalyst was placed in an XRK 900 (Anton Paar) reaction chamber equipped with a NiCr-NiAl thermocouple to measure the temperature directly next to the sample surface. The samples were first dehydrated in 12.5% O_2/N_2, cooled to room temperature, and subsequently treated in 5% H_2/Ar. The samples were then heated in 100 °C steps up to 900 °C, with an equilibration time of 30 minutes at each temperature. They were measured for 10 minutes in a 2θ range from 20-70° with a step-width of 0.025° for each step. Rietveld analysis was performed between 750 and 900 °C using the TOPAS software together with reference structures from the ICSD database. The background was corrected by using a Chebychev function with ten polynomials.

Results and Discussion

Figure 1 depicts the reducibility behavior of ceria-supported vanadia and bare ceria from TPR experiments performed between 50 and 850 °C, using a TCD to measure the hydrogen consumption (Figure 1a). Extensive spectroscopic characterization of the samples is given elsewhere.[18] V_2O_5 was employed as a well-known reference to calibrate the temperature axis.[33] For further analysis of the reducibility behavior, the hydrogen consumption during TPR was integrated (see Figure 1b).

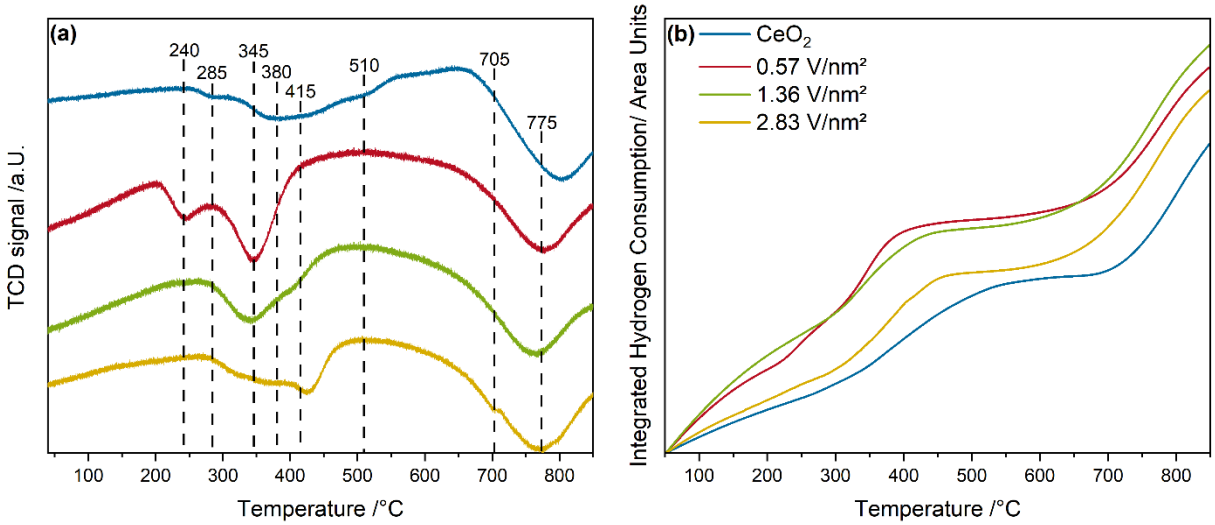

Figure 1: (a) TPR results of bare ceria and vanadia-loaded samples recorded with a heating rate of 5K/min in 7.5% H_2/Ar between 50 and 850 °C. The temperature axis was calibrated by using V_2O_5 as a reference sample (see Figure S1). Temperatures at which maxima in hydrogen consumption were detected are marked. **(b)** Integrated hydrogen consumption. The baseline correction is described in the experimental section.

As can be seen from Figure 1a, all samples show two distinct regions of hydrogen consumption, a low temperature one and a high temperature one. The low temperature region is located between 200 and 500 °C and even though the vanadia loading for all samples is relatively low, this region still varies significantly between different loadings. Bare ceria shows a very broad feature with a maximum at 380 °C, with two distinct shoulders at 285 and 510 °C indicating different contributions to the reduction behavior. The sample loaded with 0.57 V/nm² reveals a very different low-temperature region where the observed hydrogen consumption is shifted to significantly lower temperatures, with two distinct features at 240 and 345 °C, indicating

that the sample becomes much more reducible even for small vanadia loadings. For higher-loaded samples with 1.36 and 2.83 V/nm², the feature at 240 °C is absent and the feature at 345 °C decreases in intensity. Interestingly, a new feature appears at 415 °C, which becomes dominant for the sample loaded with 2.83 V/nm², indicating that there is a strong dependency on the vanadia loading. Such a splitting between different features within the low-temperature region was previously observed in VO_x/CeO_2 TPR and has been attributed to surface reduction at lower temperatures and subsurface/bulk reduction at higher temperatures.[22,30] The high temperature region starts at around 650 °C and is similar for all vanadia loadings. There is one distinct maximum, which for bare ceria is located at 805 °C but shifts to lower temperatures with increasing vanadia loading. For the sample with the highest loading, an additional shoulder can be observed at 705 °C, indicating additional contributions for the sample with the highest loading.

The integrated hydrogen consumption shown in Figure 1b appears quite similar and indicates that the general reduction behavior of VO_x/CeO_2 resembles that of bare ceria but it reveals significant differences regarding the overall amount of consumption and the temperatures at which some of the processes start to occur. The differences in the amounts of consumed hydrogen are especially large at the temperatures below 230 °C. Even though no distinct peaks are observable in this region, a constant hydrogen consumption is still observed, as can be seen from the different slopes below 230 °C in Figure 1a. A constant reduction process between 45 and 230 °C is therefore expected for all four samples, but different amounts of hydrogen are consumed, which is likely to be caused by a change in reducibility. For bare ceria and the 2.83 V/nm² sample there is low hydrogen consumption below 250 °C, whereas for the 0.57 and 1.36 V/nm² samples a much steeper increase can be observed, indicating the presence of reduction processes even at temperatures below the first TPR peaks (see Figure 1a). The sample loaded with 0.57 V/nm² shows the strongest consumption of hydrogen below 420 °C, which plateaus afterwards and stays constant up to ~600°C. The remaining samples show a similar behavior, but the temperature at which the plateau is reached increases to 460 °C (1.36 V/nm²), 480 °C (2.83 V/nm²), and 590 °C (CeO_2). Even though ceria continues to consume hydrogen up to much higher temperatures, the overall amount of consumed hydrogen is still lower at 590 °C compared to the vanadia-loaded samples. This indicates that low vanadia loadings increase the reducibility in the low temperature region significantly, which then starts to drop off

again for higher vanadia loadings. After the plateau, the samples continue to consume hydrogen at higher temperatures, beginning at ~600 °C for the 0.57 and 1.36 V/nm² samples, at 615 °C for the 2.83 V/nm² sample, and at 675 °C for bare ceria. The high temperature region is very similar in shape and overall amount of consumed hydrogen for all four samples, indicating that the reduction behavior above 600 °C is much less affected by the vanadia loading than the low temperature region. At 850 °C, the overall amount of consumed hydrogen is lowest for ceria, followed by the 2.83 V/nm² sample and the 0.57 V/nm² and 1.36 V/nm² samples, which show a similar overall consumption.

To gain a detailed understanding of the reduction behavior observed in TPR, we investigated the samples with different spectroscopic methods. A good initial descriptor of the reduction of ceria is the F_{2g} red-shift, which is determined here from Vis-Raman spectra (at 514 nm) because visible excitation allows a higher depth of penetration[18] in comparison to UV wavelengths and therefore increased sensitivity towards subsurface/bulk contributions. The F_{2g} position is an excellent descriptor for subsurface/bulk reduction due to the ceria lattice expansion upon Ce^{3+} formation during reduction.[34] Figure 2 exemplarily depicts the F_{2g} mode of ceria loaded with 1.36 V/nm² at different temperatures in 7.5% H_2/Ar (see Figure 2a) and the F_{2g} red-shifts determined by fitting analysis for all samples (see Figure 2b). For the full-range Vis-Raman spectra at each temperature as well as the evolution of the F_{2g} positions, please refer to the SI (see Figures S2 and S3).

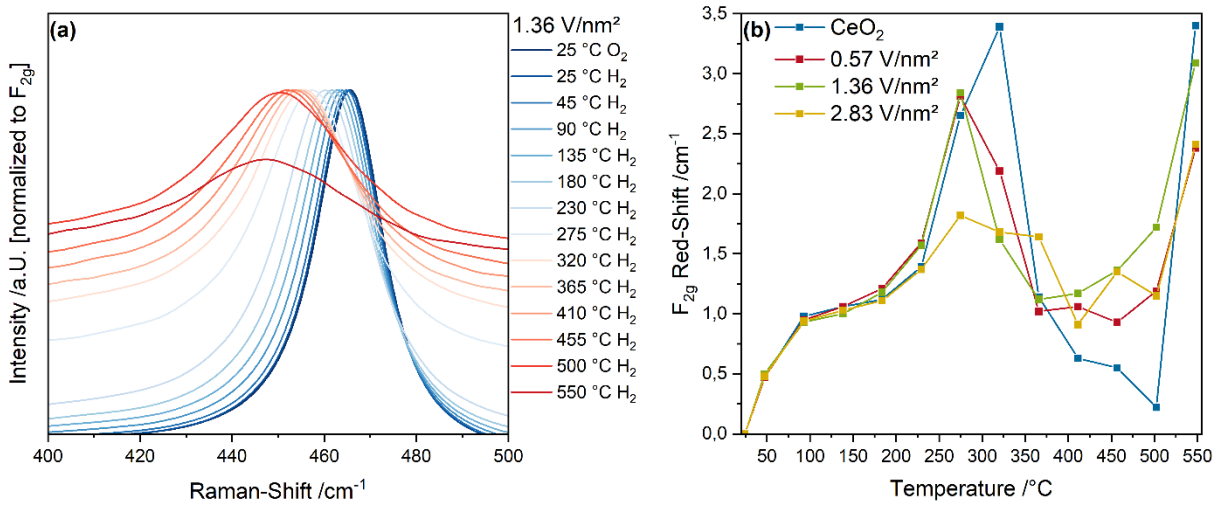

Figure 2: (a) Evolution of the F_{2g} peak for the 1.36 V/nm² sample between 25 °C and 550 °C in 7.5% H_2/Ar. **(b)** Summary of observed F_{2g} red-shifts between 25 and 550 °C for VO_x/CeO_2 samples and bare ceria. The positions were determined from in situ 514 nm Raman spectra. Please refer to the SI for full-range spectra and F_{2g} peaks.

As can be seen from Figure 2a, the F_{2g} mode shows a continuous red-shift towards a lower wavenumber with increasing temperature. The observed F_{2g} shifts are significant, considering the degree of bulk reduction needed for a shift of multiple wavenumbers.[5,32] Interestingly, the shifts show a strong variation with temperature, with a maximum between 200 and 350 °C. Such a behavior would not be expected from a pure temperature effect. Furthermore, the full width at half maximum (FWHM) steadily increases with increasing temperature up to 550 °C, which is also indicative of strongly defective ceria.[40]

Performing a fitting analysis to determine the F_{2g} maximum allowed the shifts to be quantified, as shown in Figure 2b (please see experimental section for details). Between 25 and 90 °C rather small shifts between 0 and 1 cm^{-1} are observed, and up to 180 °C the shift stays constant at about 1 cm^{-1} with each temperature step, indicating that these effects are caused by the temperature increase.[41] After that, a significant increase of the observed red-shifts occurs, starting at 230 °C with ~1.5 cm^{-1} for all samples, which increases to a maximum of 3.5 cm^{-1} at 320 °C for bare ceria and to slightly smaller maxima of 2–3 cm^{-1} at 275 °C for the vanadia-loaded samples. Only the 2.83 V/nm² sample does not show a clearly defined maximum but rather a plateau at 1.5 and 2 cm^{-1} between 275 and 365 °C, indicating a rather constant rate of reduction over a broad temperature range, which is consistent with the observed TPR behavior.

This might be caused by the increased variety of surface vanadia species with different nuclearities, which may show differing reduction behavior and interaction with the support, thereby affecting the support reduction properties, as shown previously.[26,27] Thus, the reduction behavior is strongly altered at temperatures below 450 °C depending on the distribution of vanadia species on the surface, consistent with the TPR results.

After this maximum, bare ceria shows a significant decrease in its red-shift down to almost 0 cm^{-1} at 500 °C, followed by a rapid increase to almost 3 cm^{-1} at 550 °C. This indicates the onset of an additional reduction process discussed below. For the vanadia-loaded samples a similar drop in the F_{2g} red-shift is observed between 400 and 500 °C, but to a lesser extent than for bare ceria, reaching a minimum of ~1cm^{-1} per temperature step. Consequently, at these temperatures, the VO_x/CeO_2 samples are more strongly reduced than bare ceria, which may also be related to the changed reduction behavior caused by the presence of surface vanadia and ceria's tendency to re-oxidize vanadium.[18,22,24–27,30] Between 500 and 550 °C, the vanadia-loaded samples also show a massive increase in the F_{2g} red-shift, comparable to bare ceria, indicating similar reduction processes. Therefore, similar to the TPR results, two distinct reduction regions at ~300 °C (low temperature region) and 550 °C (high temperature region) can be observed for VO_x/CeO_2 and bare ceria for the subsurface/bulk of the samples, as indicated by the F_{2g} red-shifts. This leads to the conclusion that the overall reduction behavior of the samples can be separated into surface reduction processes (<275 °C) and subsurface/bulk reduction processes (≥275 °C), both occurring in the low temperature region, as well as additional reduction processes at above 500 °C. The surface reduction is evidenced by a small but significant hydrogen consumption in the TPR below 275 °C (see Figure 1). Such a small amount of consumed hydrogen would be consistent with surface reduction due to its small content of oxygen species in comparison to the overall amount of oxygen present in the catalyst. In the following, the discussion of the reduction behavior will be separated into surface, subsurface, and bulk reduction.

Starting with the investigation of surface reduction processes, Figures 3 a and b depict UV-Raman spectra (385 nm excitation) at selected temperatures for bare ceria and the 1.36 V/nm² sample. The Raman spectra of all samples at all temperatures are shown in Figure S4. The region beyond 1100 cm^{-1} only contains the 2LO peak and is

therefore not relevant for the analysis. A summary of the peak assignments is given in Table 1.

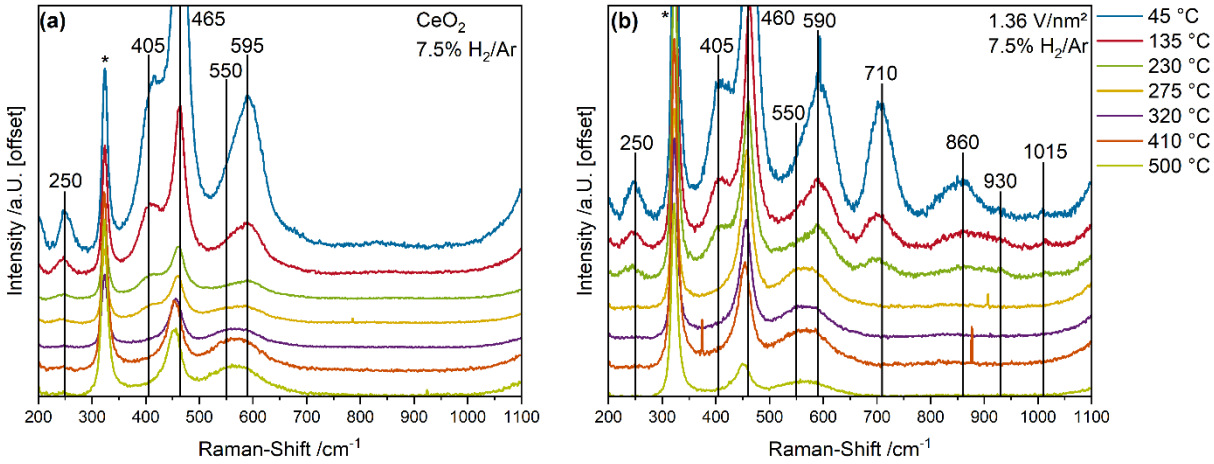

Figure 3: In situ UV-Raman spectra (385 nm excitation) of bare ceria **(a)** and the 1.36 V/nm² sample **(b)** recorded in 7.5% H_2/Ar flow at selected temperatures between 45 °C and 500 °C. The asterisk marks the signal from the used CaF_2 window.

Table 1: Peak assignments for the UV-Raman spectra.

Position /cm^{-1}	Assignment	Reference
250	Longitudinal Ce-O surface phonon (2TA contribution)	5
405	Transversal Ce-O surface phonon	5
465	F_{2g}	42
550	Defects (contribution from $V_{\ddot{O}}$)	6
595	Defects (Contribution from Ce^{3+})	6
710	V-O-Ce	22
860	V-O-Ce	22
930	V-O-V	22
1015	V=O	22

The overall intensity of the ceria signals shows a decrease with increasing temperature during the treatment in H_2/Ar, as observed before.[43,44] Therefore, further analysis of the peak intensities discussed below will be in relation to the F_{2g} peak area to ensure better comparability. For bare ceria, phonons are located at 250–600 cm^{-1}, including

the longitudinal and transversal surface phonons at 250 and 405 cm^{-1}, respectively, which first stay constant in intensity in comparison to the F_{2g} mode, then start to show a decrease in intensity at 275 °C, and finally disappear completely at 320 °C. As the decrease in surface phonon intensity is observed, the oxygen vacancy contribution in the defect region at 550 cm^{-1} starts to increase in intensity and becomes as intense as the Ce^{3+} contribution at 595 cm^{-1}. From there, both features increase equally, reaching their highest intensity compared to the F_{2g} mode at 500 °C. This behavior indicates that oxygen vacancies on the surface are first created at around 275 °C, when both the surface phonon intensity decreases and the oxygen vacancy contribution in the defect region increases. From there on, oxygen vacancies are continuously produced with increasing temperature, while oxygen is also transported from the ceria bulk to the surface (see F_{2g} shifts in Figure 2), as oxygen becomes quite mobile in ceria at elevated temperatures.

In comparison, the spectra of the 1.36 V/nm² sample reveal additional features from surface vanadia species, located between 710 and 1050 cm^{-1} (see Figure 3b). The V=O peak shows only a very small intensity at the chosen excitation wavelength and will therefore be discussed below in the context of the 514 nm Raman data. The V-O-Ce features at 710 and 860 cm^{-1} are reduced significantly in their intensities between 45 and 130 °C, continuing up to 230 °C for the 710 cm^{-1} feature. The transversal Ce-O surface phonon also decreases in intensity, but to a lesser extent than the vanadia features and slightly changes its line shape between 135 and 230 °C during the strong reduction of V-O-Ce. This smaller decrease in intensity is probably caused by ceria regenerating some of the reduced vanadia back to oxidation state V^{5+}, thereby consuming some of the lattice oxygen. At 275 °C the surface phonon completely disappears, indicating strong reduction of the ceria surface about 45 °C below the temperature at which the phonon fully disappeared on bare ceria. Concurrently, all vanadia-related peaks disappear, as they cannot be kept in oxidation state V^{5+} by ceria's lattice oxygen anymore and the oxygen vacancy contribution in the defect region increases. Reduced vanadia in oxidation state $V^{3+/4+}$ has a significantly lower Raman scattering cross section than V^{5+}, which results in the disappearance of the V^{5+}-related signals from the UV-Raman spectra.[28,45]

At temperatures above 275 °C, the vanadia-loaded sample appears to behave in the same way as bare ceria. The first maximum in the F_{2g} shifts (see Figure 2b) occurs at the same temperature as the complete disappearance of the Ce-O surface

phonon signal and the significant intensity increase in the defect region of the UV-Raman spectra. Therefore, the reduction observed on the surface (see Figures 3a and b) is also observable in the subsurface/bulk of the material due to oxygen diffusion to the catalyst surface. The maxima for the vanadia-loaded samples are also observed at 275 °C instead of 320 °C, supporting the interpretation of indirect ceria reduction mediated by vanadia reduction and subsequent re-oxidation by the ceria surface. As vanadia structures can be well reduced below 275 °C and ceria keeps vanadium in the oxidation state V^{5+}, the surface can be reduced at lower temperatures, where it is not as easily regenerated by oxygen from the ceria bulk due to the lower rate of diffusion at lower temperatures. When both samples are in a reduced state at higher temperatures (i.e., ≥320 °C), a balance between the increased rate of reduction by H_2 and the increased rate of oxygen diffusion from the bulk seems to be reached. The general trends are the same for the 0.57 V/nm² and 2.83 V/nm² samples. These results provide important first insights into the surface reduction behavior and the interaction between vanadia, the ceria surface and the subsurface. These reduction processes occur at temperatures that are consistent with the early reduction observed in TPR below 230 °C, where mainly vanadia seems to be reduced, thereby indirectly reducing ceria via the regeneration process. The intensity decrease cannot be directly correlated to the hydrogen consumption due to the potential presence of resonance Raman effects, which may selectively enhance some of the signal intensities, but qualitative trends can be derived. Between 275 and 320 °C the first strong hydrogen consumption signals can be observed in TPR, which are consistent with the complete reduction of surface lattice oxygen as indicated by the surface phonons in UV-Raman spectra.

To explain the early surface reduction behavior of bare ceria when no vanadia is present, Figure 4 exemplarily shows the Ce-OH region of bare ceria and the 1.36 V/nm² sample at temperatures between 25 and 320 °C, as an indicator for ceria surface reduction below the temperatures of vacancy formation.

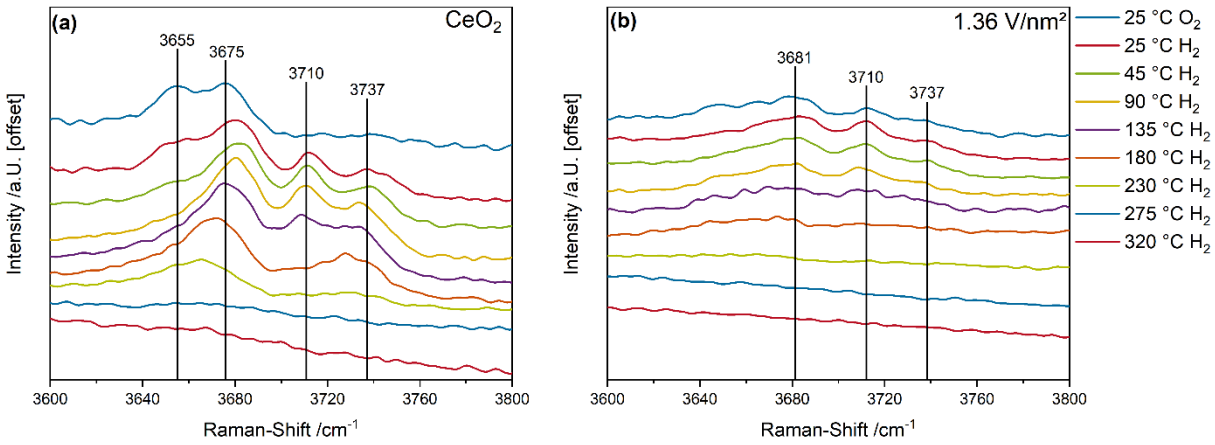

Figure 4: In situ Vis-Raman spectra (514 nm excitation) of the Ce-OH region between 25 °C and 320 °C for bare ceria **(a)** and the 1.36 V/nm² sample **(b)** in 7.5% H_2/Ar. Spectra are offset for clarity.

Compared to the vanadia-loaded sample, bare ceria shows much more pronounced Ce-OH signals, as the vanadia species anchor to ceria Ce-OH groups during the synthesis.[18,22] As discussed in the following, the reduction of Ce-OH can readily explain why ceria shows some hydrogen consumption during TPR (see Figure 1) at <230 °C although no vanadia is present. For bare ceria, at room temperature in 12.5% O_2/He flow, two Ce-OH peaks are observed at 3655 and 3675 cm^{-1}, which have been assigned to bridged Ce-OH bonds on the clean ceria surface (type II-A) and bridged Ce-OH bonds next to an oxygen vacancy (type II*-B), respectively, as some oxygen vacancies are always present on the ceria surface.[46] Upon exposure to 7.5% H_2/Ar at the same temperature, two additional Ce-OH peaks appear at 3710 and 3737 cm^{-1}, which according to the literature can be assigned to type II-B Ce-OH groups and singly bound Ce-OH bonds (type I-A), respectively.[46] The occurrence of additional Ce-OH peaks at 25 °C upon hydrogen exposure indicates the activation of hydrogen at very low temperatures, which is very different to the activation behavior of other reactants such as ethanol or propane, which are only activated at much higher temperatures.[12,13,18] When the temperature is increased, the peak at 3655 cm^{-1} decreases significantly at 45 °C and fully disappears at 90 °C, indicating that Ce-OH groups on the clean ceria surface are rather easily reduced. The peak at 3675 cm^{-1} stays constant in intensity up to 135 °C, starts to decrease at 180 °C and finally disappears at 275 °C. The type II-B Ce-OH signal located at 3710 cm^{-1} is reduced within the same temperature range, whereas the singly bound Ce-OH groups first increase in their relative intensity up to 90 °C and then start to decline until their

disappearance at 275 °C. At 275 °C and above, the Ce-OH groups are all fully reduced, which is consistent with the TPR results, where ceria shows a small but constant hydrogen consumption up to 285 °C, where it starts to show the first hydrogen consumption peak, explaining the surface reduction behavior at temperatures below oxygen vacancy formation. In comparison, vanadia barely shows any Ce-OH groups, so that their contribution to the overall reduction behavior is expected to be negligible compared to the vanadia contribution.

To understand the different vanadia surface reduction processes as indicated by their different hydrogen consumptions during TPR below 230 °C, the vanadyl region was analyzed in more detail between 25 and 275 °C (see Figure 5).

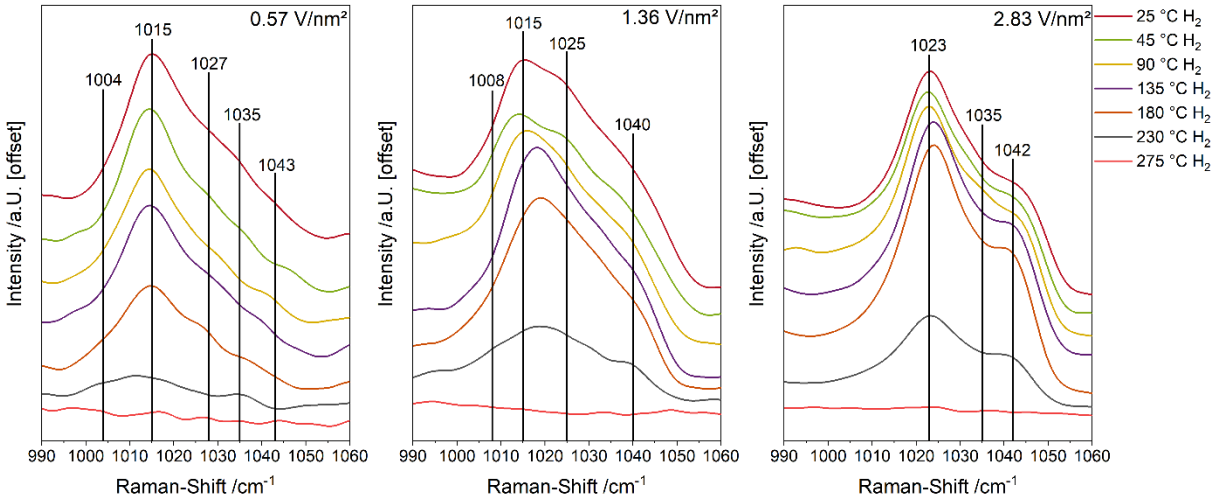

Figure 5: In situ Vis-Raman spectra (514 nm excitation) of the vanadyl region between 25 °C and 275 °C for VO_x/CeO_2 samples in 7.5% H_2/Ar. At higher temperatures (>275 °C) no vanadyl peak is observed. Spectra are offset for clarity and normalized to the F_{2g} peak.

In the vanadyl region of the VO_x/CeO_2 samples, multiple contributions to the overall peak can be observed at ~1005, ~1015, ~1025, ~1035, and ~1040 cm^{-1}, which originate from different vanadia nuclearities as vanadyl groups can exhibit dipole–dipole interactions. As a result, vanadia structures with higher nuclearities show larger blue-shifts, resulting in a fine structure on a ceria support. The above positions can be assigned to monomeric, dimeric, trimeric, tetrameric, and pentameric species, respectively.[13,18,47] In the following, the tetra- and pentameric species will be referred to as oligomeric vanadia species. In general, only very small changes in the vanadyl fine structure are detected below 230 °C. It needs to pointed out that very small

changes might be caused by noise, as the vanadyl intensity is comparably small (see red curves at 275 °C in Figure 5). Additionally, the reduction of V-O-V (see Figure 3) results in a decrease of the nuclearity, thereby also slightly changing the position before its regeneration by ceria. The overall shape, however, shows only insignificant changes at lower temperatures before it is more significantly reduced. As the vanadia reduction is regenerated by ceria, the reducibility of the different nuclearities should not influence the fine structure for the same sample at different temperatures, but still leads to different hydrogen consumptions due to the different ceria reduction rates mediated by the different (nuclearity-dependent) reducibilities. For the 0.57 V/nm² sample, the strongest contribution to the vanadyl peak comes from the dimeric species, whereas at higher loadings, there is a shift towards increasingly higher contributions from trimeric and oligomeric species. With increasing temperature, the vanadyl peaks appear to stay unchanged up to 230 °C, where a significant decrease in intensity is observed, but the overall line shape still stays unchanged. When the temperature is increased further to 275 °C, the vanadyl peak completely disappears, which is consistent with the other vanadia features detected by UV-Raman spectroscopy (see Figure 3) and indicates the complete reduction of vanadium(V) species on the catalyst surface. This coincides well with the subsequent creation of oxygen vacancies as observed in the UV-Raman spectra as well as the strong increase in hydrogen consumption in TPR at the same temperature.

To explain the difference in the observed hydrogen consumptions between samples with different vanadia loadings at temperatures below 230 °C, the strong shift in the distribution of nuclearities with vanadium loading seems to be of relevance. Previous DFT (density functional theory) studies already showed that there is a significant difference in the reducibility between monomeric, dimeric, and trimeric vanadia species, where the vanadyl oxygen is easily reduced for monomeric and dimeric species, whereas trimeric vanadyl oxygen is not as easily reduced.[26] This finding, in combination with the observed vanadia nuclearity distributions, can explain the difference in reduction behavior, as the two samples with significant monomeric and dimeric contributions show significantly more hydrogen consumption below 230 °C compared to the 2.83 V/nm² sample, which contains mostly trimeric and oligomeric species, leading to much less hydrogen consumption at these temperatures.

The difference between the onset temperatures for the first hydrogen consumption peak (see Figure 1) can also be explained by the different distribution of

surface vanadia species. Vanadia changes the reducibility of ceria surface oxygen species in close proximity to the vanadia species, whereby ceria lattice oxygen atoms next to monomeric and dimeric species are more easily reduced than those close to trimeric species.[26,27] Due to the decreasing relative amount of monomeric and dimeric species with increasing vanadia loading, the temperature at which the ceria surface lattice oxygen is first reduced is lowest for the 0.57 V/nm² sample and steadily increases with increasing loading. The hydrogen consumption signal for the 0.57 V/nm² sample is also sharper than that of the more highly loaded samples, as there is a sharp distribution of different surface species. As the samples with higher vanadia loadings contain a broader distribution of species, the hydrogen consumption signal also broadens, as the different species influence the reducibility differently, resulting in a variety of different vacancy formation energies. Despite this, the initial vacancy formation temperature is lower for all vanadia-loaded samples than for bare ceria, as the reduction of surface lattice oxygen is always easier in proximity to vanadia than on a clean surface.[26]

To investigate in more detail the very significant reduction step at 275 °C, where surface oxygen vacancies start to form and the V^{5+}-related signals disappear, Figure 6 depicts quasi in situ XP spectra of the V $2p_{3/2}$ region for VO_x/CeO_2 samples after treatment in 7.5% H_2/Ar and 12.5% O_2/Ar, together with the results of a fit analysis using three components (V^{3+}, V^{4+}, V^{5+}). The resulting areas for the V^{3+}, V^4 and V^{5+} contributions[48] as well as the ratios of O/Ce and V/Ce for VO_x/CeO_2 and bare ceria in 12.5% O_2/Ar and 7.5% H_2/Ar are summarized in Table 2.

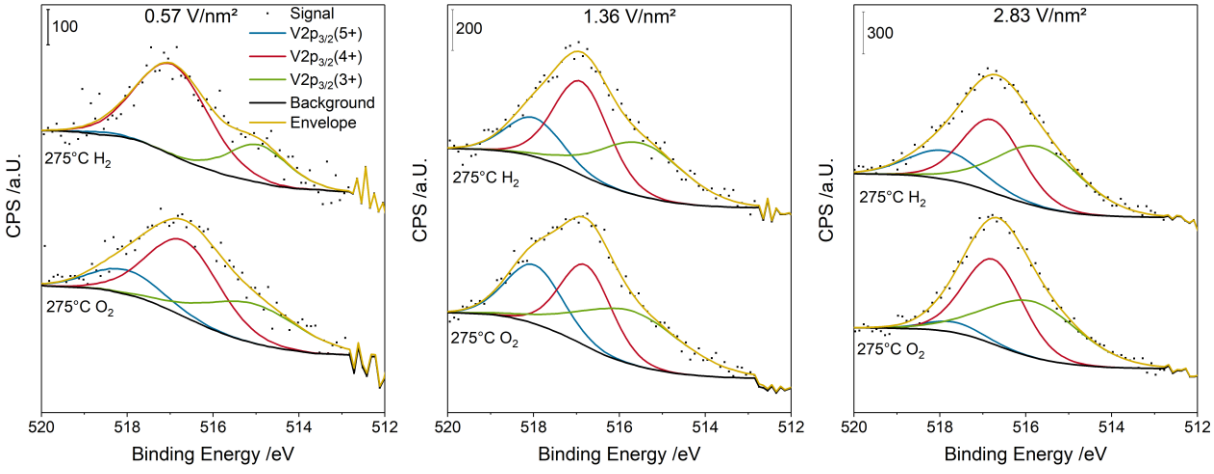

Figure 6: V $2p_{3/2}$ photoemission of VO_x/CeO_2 samples at room temperature after oxygen pretreatment (12.5% O_2/Ar) at 300 °C (bottom) and after hydrogen pretreatment (7.5 % H_2/Ar) at 300 °C (top) followed

by (air-free) transfer to the analysis chamber, together with the results of a fit analysis.[48] Spectra are offset for clarity.

Table 2: Results of the quasi in situ XPS analysis focussing on the vanadium oxide state. Spectra were recorded after pretreatments in 12.5% O_2/He and 7.5% H_2/Ar at 300 °C. For details of the analysis, please refer to the experimental section.

Sample	O/Ce	V/Ce	% V^{3+}	% V^{4+}	% V^{5+}	Oxidation State
CeO_2 O_2	1.61	--	--	--	--	--
CeO_2 H_2	1.42	--	--	--	--	--
0.57 V/nm² O_2	2.13	0.07	0.34	0.50	0.16	3.82
0.57 V/nm² H_2	2.16	0.06	0.26	0.73	0.01	3.75
1.36 V/nm² O_2	2.04	0.11	0.42	0.32	0.26	3.84
1.36 V/nm² H_2	2.60	0.13	0.39	0.43	0.18	3.79
2.83 V/nm² O_2	2.44	0.25	0.49	0.46	0.05	3.56
2.83 V/nm² H_2	2.61	0.22	0.44	0.38	0.18	3.74

Starting with bare ceria, the O/Ce ration was determined to decrease from 1.61 to 1.42 for O_2/He and H_2/Ar treatment, respectively. This is in line with expectation as the reduction of the ceria surface is accompanied with surface oxygen vacancy formation, which is consistent with the TPR results, as a first small hydrogen consumption peak is observed at 285 °C. Remarkably, for the vanadia-loaded samples, this trend is reversed. While unexpected at first sight, the observed behavior can be explained when the limited information depth of XPS is taken into account. In fact, as vanadia becomes reduced, it is re-oxidized back to oxidation state V^{5+} by ceria, leading to the creation of oxygen vacancies. This increase in the number of charge carriers increases the oxygen mobility, and due to vanadia re-oxidation, more oxygen is found in the first few sample layers, even though overall the catalyst is in a more reduced state. This trend is reproducible for all vanadia-loaded samples and is unlikely to be caused by any external effect, such as exposure to air during the transfer, since the sample was directly transferred from the gas-pretreatment cell via several pressure stages to the analysis chamber. The increase in the V/Ce ratios is in line with the increase expected due to the increase in vanadia loading from sample to sample and does not vary significantly with the type of pretreatment. This also explains the higher O/Ce ratio for

the 2.83 V/nm² sample, as more vanadium is detected within the limited information depth of XPS, leading to less detected Ce while the amount of detected oxygen stays similar, as VO_x also contains oxygen. This is also described by the V/Ce ratio that increases much more significantly from 1.36 to 2.83 V/nm² compared to the sample with the lowest loading.

Based on the results of the fit analysis shown in Table 2, the distribution of the vanadium oxidation states can be compared as a function of pretreatment and loading. Contributions from all three oxidation states are present in oxidizing as well as reducing conditions where V^{4+} becomes especially dominant. The average oxidation states are lower than for other supports such as alumina, but the significant presence of V^{4+} has been observed before.[29] For the 0.57 V/nm² sample, a decrease in the proportion of V^{5+} and of V^{3+} as well as a significant increase in the amount of V^{4+} can be observed, on comparing the spectra after O_2/Ar and H_2/Ar treatment. This indicates a disproportionation of V^{5+} and V^{3+} species to form additional V^{4+} species on the surface. As more V^{5+} than V^{3+} is consumed during disproportionation, the additional V^{5+} is likely to be reduced directly to V^{4+}, suggesting multiple channels of reduction and regeneration at the interface despite the similar average oxidation state, highlighting the complexity of the system. The increase in V^{4+} species might be caused by the unique interaction between vanadia and ceria and the higher availability of ceria lattice oxygen close to the surface during the reduction processes, before vanadia is further reduced at higher temperatures, as this behavior during initial reduction can not be observed for other supports.[29,49] The complete disappearance of V^{5+} is also in agreement with the Raman results, where no vanadia signals can be observed at 275 °C anymore (see Figures 3 and 5).

The same observations can be made for the 1.36 V/nm² sample. However, the sample with the highest vanadia loading diverges from the observed trends and decreases in its V^{3+} and V^{4+} contribution, whereas the V^{5+} contribution to the observed signal increases. This behavior differs significantly from that of the first two samples when the average oxidation state of the samples is considered. In fact, the two lower-loaded samples have similar average oxidation states after oxidizing gas-phase treatments and a slightly decreased oxidation state after hydrogen treatment (see Table 2). Nevertheless, the observed decrease is quite small, indicating that ceria can re-oxidize reduced vanadia as vanadia disproportionates and mostly consists of V^{4+} after reduction at this temperature. This is in good agreement with literature results,

where ceria is also described to keep vanadia oxidized in different gas-phases.[22,24–26] This measurement is not limited by the precision of XPS, as the average oxidation states are very similar and within the margin of error, but the individual contributions from the vanadium oxidation states vary quite significantly between the gas phases, i.e., outside the margin of error, and the results for the average oxidation state are still similar. This also coincides with the temperature at which the first oxygen vacancies are created in the ceria surfaces, indicating that vanadia is first reduced by hydrogen and then disproportionation occurs, which requires ceria lattice oxygen, leading to vacancy creation and a rather constant oxidation state. In comparison, the oxidation state in the 2.83 V/nm² sample increases from an initial value of 3.56 to 3.74, which resembles the averaged oxidation states of the other samples after hydrogen treatment but differs from its initial value under oxidizing conditions. This indicates that the different trend observed for this sample appears to be caused by the low average oxidation state after oxidizing treatment. The difference in the initial state of the sample might be caused by the high vanadia loading, which is very close to the point where three-dimensional VO_x particles form on the surface (2.9 V/nm²). If such particles were formed, one may expect part of the particles to exhibit a different electronic behavior than the (2-dimensional) surface vanadia aggregates of the other samples, leading to different oxidation states at higher loadings. It appears that upon reduction, V-O-V bonds in these particles are broken, leading to the formation of more surface-confined species, which behave similarly to those present in the samples with lower loadings, resulting in a similar average oxidation state. Notably, a loading-dependent difference in behavior can also be observed in the TPR results (see Figure 1b), where the initial reduction of the 2.83 V/nm² sample varies significantly from those of the other vanadia-loaded samples and rather resembles that of bare ceria. The change in reduction behavior is unlikely to be caused by the presence of vanadia trimers only as there are significant contributions from higher vanadia nuclearities at this loading (see Figure 5), thus providing a structural rationale for the different characteristics of the highly-loaded sample.

So far, the surface processes up to the reduction of V^{5+} and the first formation of surface oxygen vacancies have been analyzed and discussed in detail. To understand the reduction behavior at higher temperatures, bulk methods are necessary to probe subsurface and bulk processes. Furthermore, at 275 °C, most vanadium is not yet fully reduced but mainly present in oxidation state V^{4+}. With

increasing temperature, further reduction of vanadium is expected but not accessible by Raman spectroscopy, due to the low scattering cross section of reduced species, or by quasi in situ XPS, due to temperature limitations of the experimental setup. Therefore, we have explored the potential of in situ UV-Vis spectroscopy to probe vanadia as well as ceria bulk reduction. Figure 7 shows the UV-Vis spectra of CeO_2 and the 1.36 V/nm² sample in 7.5% H_2/Ar at selected temperatures. As many properties measured in UV-Vis spectra are temperature-dependent, the same temperature ramp as for the reduction with hydrogen was performed in pure helium to exclude any temperature effects. The temperature-dependent spectra of all samples in pure helium and 7.5% H_2/Ar are given in the SI (see Figures S5 and S6).

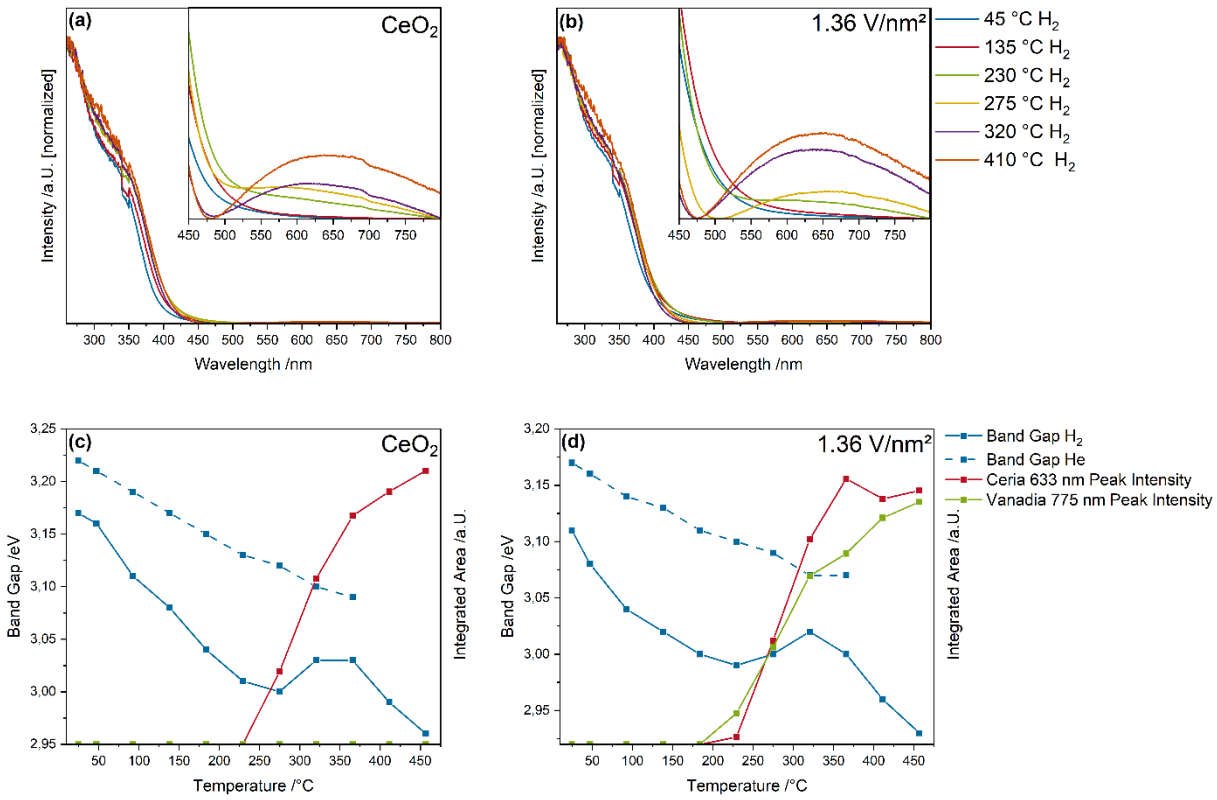

Figure 7: In situ UV-Vis spectra for bare ceria **(a)** and the 1.36 V/nm² sample **(b)** in 7.5% H_2/Ar at selected temperatures between 45 and 410 °C. The insets highlight the absorption behavior between 450 and 800 nm. From the fit analysis (see Figure S7), the areas of the $Ce^{3+} \rightarrow Ce^{4+}$ charge transfer and vanadia d-d transitions for bare ceria **(c)** and the 1.36 V/nm² sample **(d)** are obtained and compared to the determined band gaps. To exclude temperature effects, the same spectra were recorded in pure helium at the same temperatures. For details see text and the SI.

In Figures 7 a and b, in situ UV-Vis spectra for bare ceria and the 1.36 V/nm² sample are shown. Two types of spectral changes are observed: first, the band gap absorption

energy shifts towards higher wavelengths with increasing temperature, and second, a distinct absorption between 500 nm and 800 nm becomes observable for both samples. The shift in the band gap energy is caused by the formation of oxygen vacancies, which create electronic states closer to the conduction band, thereby decreasing the overall band gap.[50] The shift in band gap energy is therefore a good indicator of the overall ceria reduction. The absorption in the region between 500 and 800 nm is caused by $Ce^{3+} \rightarrow Ce^{4+}$ transitions located at around 633 nm, which is a good second indicator of reduced bulk ceria,[51,52] and by vanadia d-d transitions, which only become allowed transitions upon vanadia reduction ($V^{3+/4+} \rightarrow V^{5+}$), thus representing a good indicator for further vanadia reduction beyond V^{4+}. Since the vanadia d-d transitions are very broad, it is difficult to determine their exact position. We used 775 nm as the position of the vanadium d-d transition as determined by electron energy loss spectroscopy (EELS) on a 2D V_2O_5 material and allowed for divergence between 750 and 800 nm to account for the different material and possibly different vanadia state.[53]

The observed dynamics in the spectra were quantified using Tauc plots for the band gap and fitting analysis (exemplarily shown in Figure S7) for both transitions in the region between 500 and 800 nm. Figures 7c and d show the trends obtained for bare ceria and the 1.36 V/nm² sample, respectively. In the presence of helium, the band gap energy shows a constant red-shift with increasing temperature. The absorption in the region between 500 and 800 nm is not present in helium (see Figure S5). The observed spectroscopic changes are therefore caused by the reducing hydrogen atmosphere. As shown in Figures 7c and d, the band gap energy shows a linear decrease for both samples, which continues up to 275 °C for ceria and up to 230 °C for the 1.36 V/nm² sample. Above these temperatures, the band gap increases again and moves through a maximum, which coincides perfectly with the appearance of the $Ce^{3+} \rightarrow Ce^{4+}$ transition for both samples. The observed blue-shift of the band gap can therefore serve as an indicator of the onset of oxygen vacancy formation, as the blue-shift does not appear to be caused by actual ceria reduction (which would lead to a red-shift), but rather by the influence of the absorption at 633 nm on the Tauc analysis. These temperatures are well in line with the observed structural dynamics and vacancy formation from F_{2g} red-shifts and UV-Raman spectra.

In addition, the ceria reduction can be quantified by UV-Vis spectroscopy up to much higher temperatures than by UV-Raman spectroscopy, where the decreasing

scattering cross-section and the constant shape of the defect region make quantification rather difficult. Figures 7c and d show that ceria is strongly reduced between 250 and 400 °C, whereby the observed 633 nm absorption increases sharply before it starts to drop off at 400 °C for bare ceria, but increases more slowly and then plateaus at 400 °C for the 1.36 V/nm² sample. This behavior is roughly in line with the observed hydrogen consumptions from TPR (see Figure 1). In addition, the vanadia reduction can be probed further. The observed absorptions for d-d transitions reveal (see Figures 7c and d) that vanadia is strongly reduced when ceria is reduced. However, the absorption does not plateau at around 400 °C, but further increases up to the maximum UV-Vis temperature, which is likely to be caused by vanadia reduction down to V^{3+}, thus explaining why the vanadia-loaded samples have a higher overall hydrogen consumption than bare ceria in TPR analysis. The spectra for all four samples at all temperatures are shown in Figure S6 and the obtained trends for the band gap as well as the obtained areas from the fit analysis are shown in Figures S8 and S9.

The previously performed analysis allowed the complete TPR low-temperature region to be investigated and interpreted by spectroscopic methods. Above 500 °C, very low amounts of hydrogen are consumed up to the high-temperature region. The small consumptions of hydrogen were investigated by quasi in situ DRIFTS analysis. For that, the sample was placed in the IR reaction chamber and was pretreated in 12.5% O_2/He and 7.5% H_2/Ar. After the sample had cooled to room temperature in pure helium, an IR spectrum was measured to avoid thermal noise at the elevated temperatures.

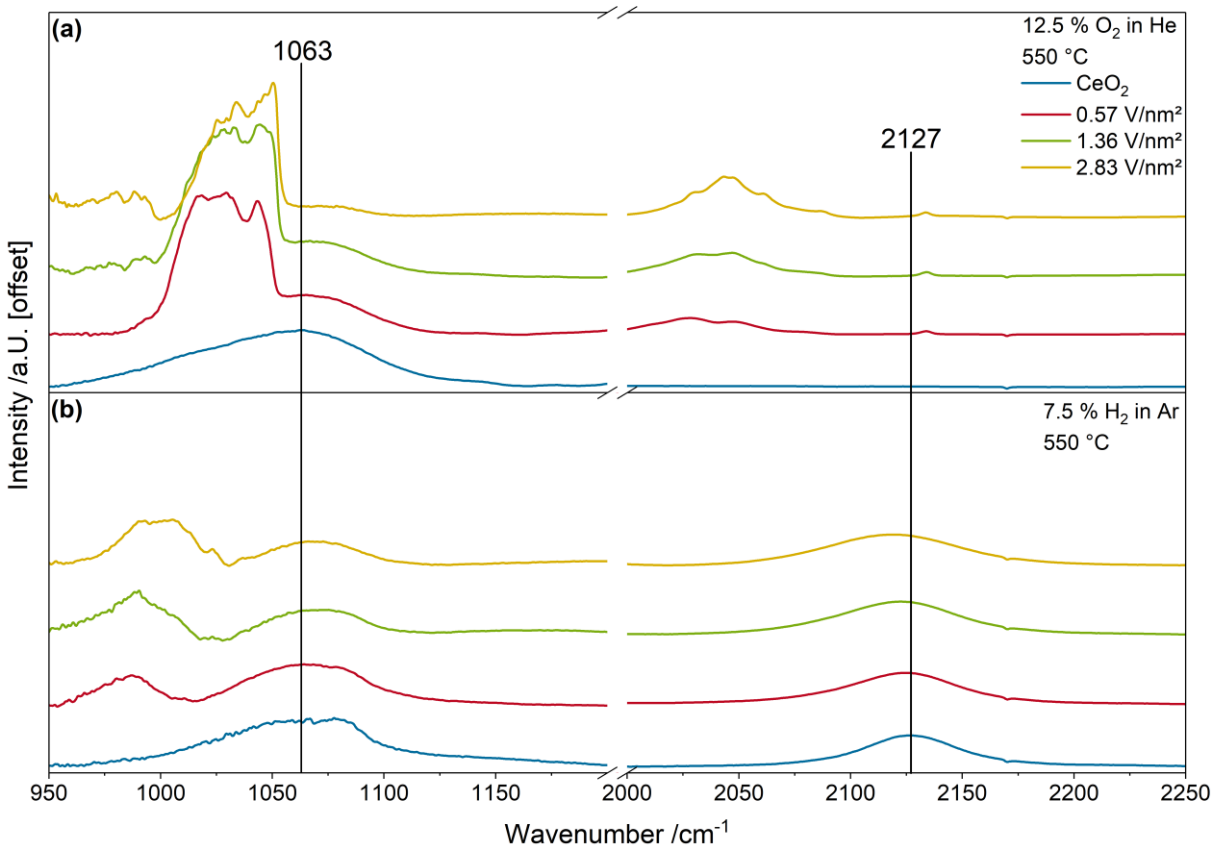

Figure 8: DRIFT spectra of bare ceria and VO_x/CeO_2 samples recorded at 25 °C after pretreatment in **(a)** 12.5% O_2/He and **(b)** 7.5% H_2/Ar and subsequent cooling down from 550 °C to 25 °C in He. The resulting spectra are offset for clarity.

Figure 8 depicts room temperature DRIFT spectra after oxidative (a) and reductive (b) pretreatment, covering the regions 900-1200 cm^{-1} and 2000-2400 cm^{-1}, where vanadyl fundamental and overtone vibrations may be expected. After oxidative pretreatment, a vanadyl peak is observed at 1000-1050 cm^{-1}. Apparently, there is an additional broad (asymmetric) feature, which overlaps with the vanadyl peak. In this wavenumber region, besides Ce-O vibrations of Ce-OH bonds also Ce-H vibrations of different surface and bulk hydrides may be located.[54] To disentangle the different contributions, we therefore examined the overtone region between 2000 and 2400 cm^{-1}. At 2127 cm^{-1} a peak is observed that would be consistent with a fourfold coordinated bulk hydride,[54] corresponding to a fundamental vibration located at 1063 cm^{-1}, where analysis is difficult due to overlap. To confirm that this assignment, we performed DRIFTS at different temperatures, as the Ce-O and vanadyl vibrations would be expected to be present at all temperatures whereas Ce-H vibrations should be observable only at high temperatures in hydrogen atmosphere. From the DRIFT spectra it can be seen that

this overtone is not present at lower temperatures but begins to appear at above 300 °C (see Figure S10). We therefore conclude bulk hydride formation to occur at above 300 °C up to 550°C, which offers an explanation for the continuous hydrogen consumption above 400 °C together with the continuous vanadia reduction for the vanadia-loaded samples (see above).

Above 550 °C, our spectroscopies become unviable due to sensitivity issues caused by the high temperature, but large hydrogen consumptions were observed in TPR at temperatures above 700 °C, indicating a phase transition. These occur between 775 and 810 °C and are consistent with the beginning phase transition into substochiometric structures which first start to appear in nanoparticles, not detected by XRD.[55,56] Only at higher temperatures, a significant change in the diffraction pattern would become apparent.[57] Only the sample with the highest loading (2.83 V/nm²) shows an additional shoulder at 705 °C (see Figure 1). Besides, the temperatures of the phase-transition are shifted towards lower values when vanadia is present. To determine the cause of the shoulder for the 2.83 V/nm² sample, in situ XRD was performed in 5% H_2/Ar to determine any additional phase-transitions besides the one mentioned above.

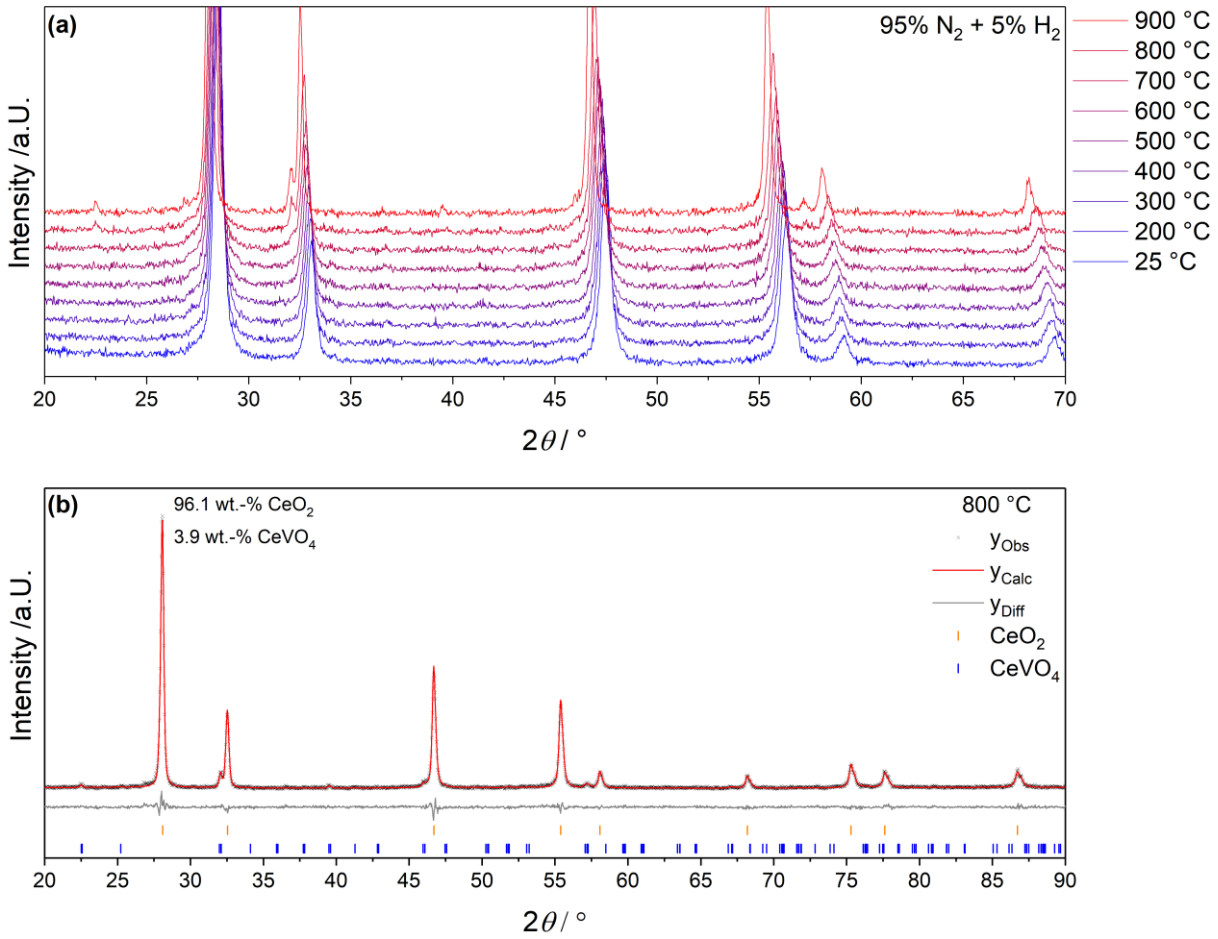

Figure 9: In situ XRD diffraction patterns for the 2.83 V/nm² sample **(a)** measured in 5% H_2/N_2 at 25 °C and in 100 °C steps between 200 and 900 °C. **(b)** Rietveld fit (red) performed on the diffractogram (black) collected at 800 °C.

Figure 9 depicts temperature-dependent diffractograms of the 2.83 V/nm² samples together with the results of a Rietveld analysis based on the diffractogram at 800 °C. Up to 600 °C the diffractograms reveal no differences and show only a slight shift of the reflections peaks towards lower angles due to the increased temperatures. At 700 °C, small changes start to become apparent at 22, 32 and 57° *2θ* where additional reflections appear. When the temperature is further increased, these reflections gain in intensity and coincide well with the positions expected for $CeVO_4$ that has been reported to be formed in the presence of high vanadium loading (starting at 1 V/nm² at high temperatures under reducing conditions, but much more significant amounts are formed at ~3 V/nm²) or under reducing conditions.[22,25] To quantify the amount of $CeVO_4$ present under these conditions, Rietveld analysis was performed for the diffractogram at 800 °C, yielding 3.9% $CeVO_4$. This is a significant amount, which

is likely to cause some measurable degree of hydrogen consumption, leading to the formation of the shoulder observed for the sample with the highest vanadia loading (2.83 V/nm²). For the other VO_x/CeO_2 samples, such a reaction is not observed because the vanadium loading is too low at 0.57 and 1.36 V/nm² in the measured temperature range.

Figure 10 summarizes the above findings and bridges the gap between the observed hydrogen consumptions and the interpretations on a molecular level, thus allowing the hydrogen consumption behavior in the TPR to be assigned to different structural changes, including the influence of the vanadia loading. The bars indicate the temperature range for each process which was determined exclusively by our spectroscopic findings and show a very good agreement with the observed hydrogen consumptions. The designations of surface Ce-OH and surface vanadia refer to initial Ce-OH and vanadia reduction regenerated by ceria, respectively, determined from UV- and Vis-Raman spectra (see Figures 3-5). Surface defect formation is caused by the depletion of surface oxygen and the permanent formation of oxygen vacancies on the surface as analyzed by UV-Raman spectroscopy (see Figure 3 and S4), and bulk defects are caused by the diffusion of bulk oxygen to the sample surface and subsequent reduction which was determined from Vis-Raman and UV-Vis spectra (see Figures 2, 3, 7, and S9). Strong vanadia reduction refers to the continued reduction of vanadia from V^{4+} to V^{3+} and starts after V^{5+}-related signals disappeared from the Raman spectra. The continued reduction was determined by XP and UV-Vis spectroscopy (see Figures 6 and 7). For the 0.57 V/nm² sample, there is not enough vanadium present to detect this feature using TPR, as the hydrogen consumption for this reduction process is very small, even for the 1.36 V/nm² sample. Hydride formation is tracked by temperature-dependent DRIFTS measurements (Figures 8 and S10) but its contribution to the overall hydrogen consumption is expected to be comparably small as the TPR shows only small hydrogen consumptions without any maxima in this temperature range. Finally, the phase transitions were determined using in situ XRD (see Figure 9) but no temperature range is given as no additional processes were determined to occur in this temperature range and therefore, the observed hydrogen consumption are attributed to the occurring phase transitions.

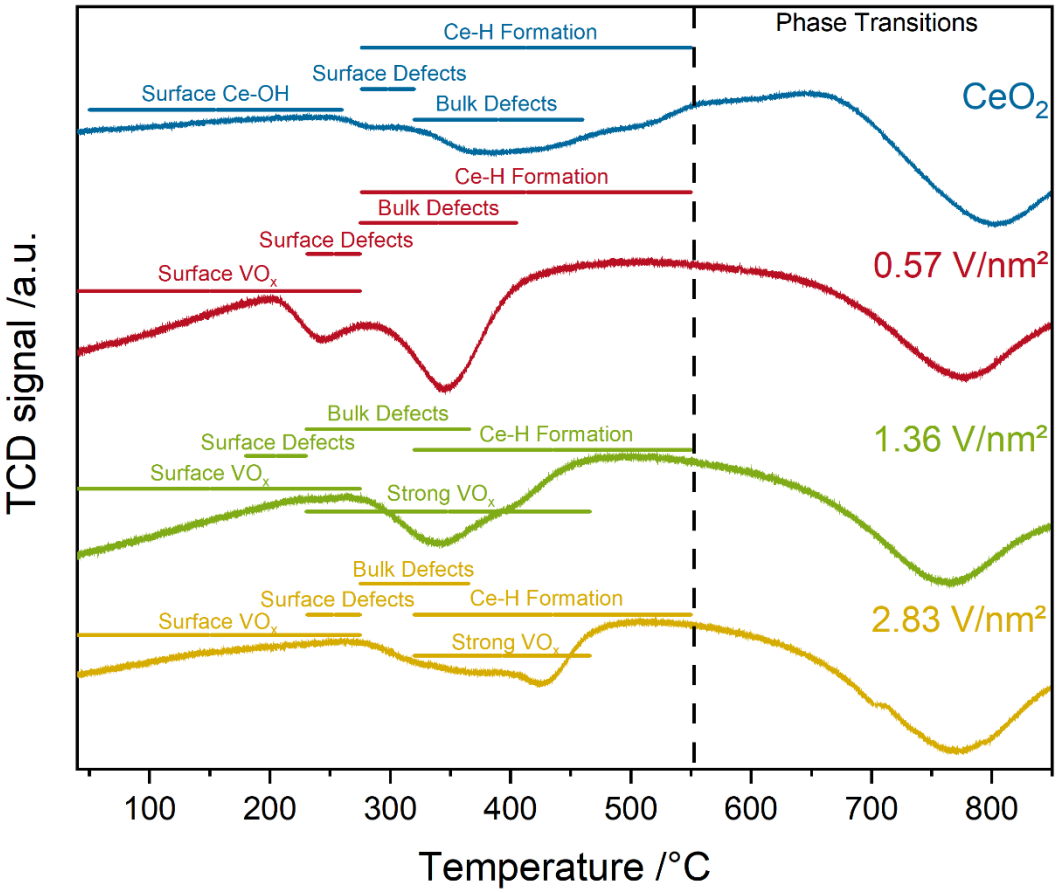

Figure 10: Insight into the structural changes during TPR of bare ceria and vanadia-loaded samples, based on temperature-dependent analysis by multiple in situ spectroscopy and in situ diffraction. For details refer to the text.

Conclusion

In this study we link the reducibility, an important property of metal-oxide catalysts accessible by temperature-programmed reduction (TPR), to molecule-based processes, as developed by the application of multiple in situ methods. It is shown that a detailed understanding of the surface, subsurface and bulk dynamics during temperature-dependent reduction is strongly facilitated by complementary analysis using spectroscopy and diffraction.

The TPR of VO_x/CeO_2 catalysts and bare ceria as a reference sample reveals that the hydrogen consumptions can be separated into a high temperature region and a low temperature one, whereby the low temperature region shows multiple contributions and significant variations between different vanadia loadings. In the high temperature region, a rather similar behavior is observed, and the position of the maximum hydrogen consumption is located at temperatures, where first phase-transitions into nano dispersive sub-stoichiometric phases can appear. Vis-Raman spectra, employed to further separate the processes in the low temperature region, reveal surface and subsurface/bulk contributions.

Surface contributions at temperatures below 230 °C were determined to be caused by Ce-OH reduction for bare ceria, where bridged Ce-OH groups next to vacancies and singly bound Ce-OH groups were the most important, as well as early vanadia reduction, which is regenerated by ceria to keep vanadium in oxidation state 5+. Further reduction at higher temperatures is caused by oxygen depletion in the ceria surface and surface vacancy formation as well as vanadia reduction by disproportionation of V^{3+} and V^{5+} species to V^{4+} species. All reduction processes occur at different temperatures for different vanadia loadings, and the surface vanadia structures, as determined by the vanadyl fine structure, significantly influence the overall reduction behavior.

Beyond surface reduction ceria subsurface and bulk oxygen atoms diffuse to the surface, where they become reduced and bulk oxygen vacancies are formed. For vanadia-loaded samples, concurrently, strong vanadia reduction to oxidation states lower than V^{4+} occurs and leads to an overall higher hydrogen consumption for vanadia-loaded samples than for bare ceria. These processes are overlapped by the formation of Ce-H bulk hydrides, which add to the overall hydrogen consumption up to 550 °C. At even higher temperatures, the beginning of phase transitions towards sub-stoichiometric nano-dispersive phases can be observed for all samples but for the

sample with the highest loading, first a partial phase transition from CeO_2 to $CeVO_4$ is observed. It is demonstrated that the temperature, at which the reduction processes occur, is strongly determined by the vanadium loading because the changes in vanadia structure with increasing loading and the different structures are characterized by different reducibilities.

In summary, we present the first comprehensive study in which the reduction properties of ceria and different VO_x/CeO_2 samples are investigated with multiple in situ methods over a temperature range of 800 °C and used for the interpretation of TPR results. With our approach, it is possible to also interpret in detail the TPR results of other important catalytic materials and allow for a molecular interpretation of the easily accessible reducibility behavior, thus facilitating the link between mechanistic research and technical application. This approach can readily be transferred to other important catalytic materials such as TiO_2 or SiO_2, which are already used in technical applications and to different properties accessible by, for example, temperature-programmed oxidation (TPO), temperature-programmed adsorption/desorption (TPD) or temperature-programmed reaction (TPR), making this approach highly and broadly applicable in the field of metal-oxide catalysis.

Declaration of Competing Interest

The authors declare that they have no known competing financial interests or personal relationships that could have appeared to influence the work reported in this paper.

Acknowledgements

The authors acknowledge Dr. Martin Brodrecht for performing nitrogen adsorption experiments and BET analysis. This work was supported by the Deutsche Forschungsgemeinschaft (DFG, HE 4515/11-1)

Supporting Information

The supporting information to this article contains additional TPR data, in situ Raman, UV-Vis and DRIFT spectra, as well as results from further analyses.

References

(1) Bond, G. C. *Heterogeneous catalysis*; Oxford University Press,New York, NY, 1987.

(2) Beck, B.; Harth, M.; Hamilton, N. G.; Carrero, C.; Uhlrich, J. J.; Trunschke, A.; Shaikhutdinov, S.; Schubert, H.; Freund, H.-J.; Schlögl, R., et al. Partial oxidation of ethanol on vanadia catalysts on supporting oxides with different redox properties compared to propane. *J. Catal.* **2012**, *296*, 120–131. DOI: 10.1016/j.jcat.2012.09.008.

(3) Carrero, C. A.; Schloegl, R.; Wachs, I. E.; Schomaecker, R. Critical Literature Review of the Kinetics for the Oxidative Dehydrogenation of Propane over Well-Defined Supported Vanadium Oxide Catalysts. *ACS Catal.* **2014**, *4* (10), 3357–3380. DOI: 10.1021/cs5003417.

(4) Zhouxin Luo; Guoqiang Zhao; Hongge Pan; Wenping Sun. Strong Metal–Support Interaction in Heterogeneous Catalysts. *Adv. Energy Mater.* **2022**, *12* (37), 2201395. DOI: 10.1002/aenm.202201395.

(5) Schilling, C.; Hofmann, A.; Hess, C.; Ganduglia-Pirovano, M. V. Raman Spectra of Polycrystalline CeO_2 : A Density Functional Theory Study. *J. Phys. Chem. C* **2017**, *121* (38), 20834–20849. DOI: 10.1021/acs.jpcc.7b06643.

(6) Filtschew, A.; Hofmann, K.; Hess, C. Ceria and Its Defect Structure: New Insights from a Combined Spectroscopic Approach. *J. Phys. Chem. C* **2016**, *120* (12), 6694–6703. DOI: 10.1021/acs.jpcc.6b00959.

(7) Filtschew, A.; Hess, C. Unravelling the mechanism of NO and NO_2 storage in ceria: The role of defects and Ce-O surface sites. *Appl. Catal. B: Environ.* **2018**, *237*, 1066–1081. DOI: 10.1016/j.apcatb.2018.06.058.

(8) Hu, X.; Chen, J.; Qu, W.; Liu, R.; Xu, D.; Ma, Z.; Tang, X. Sulfur-Resistant Ceria-Based Low-Temperature SCR Catalysts with the Non-bulk Electronic States of Ceria. *Environ. Sci. Technol.* **2021**, *55* (8), 5435–5441. DOI: 10.1021/acs.est.0c08736. Published Online: Mar. 16, 2021.

(9) Ziemba, M.; Hess, C. Influence of gold on the reactivity behaviour of ceria nanorods in CO oxidation: combining operando spectroscopies and DFT calculations. *Catal. Sci. Technol.* **2020**, *10* (11), 3720–3730. DOI: 10.1039/D0CY00392A.

(10) Ziemba, M.; Weyel, J.; Hess, C. Elucidating the mechanism of the reverse water–gas shift reaction over Au/CeO_2 catalysts using operando and transient spectroscopies. *Appl. Catal. B: Environ.* **2022**, *301*, 120825. DOI: 10.1016/j.apcatb.2021.120825.

(11) Lin, L.; Yao, S.; Liu, Z.; Zhang, F.; Li, N.; Vovchok, D.; Martínez-Arias, A.; Castañeda, R.; Lin, J.; Senanayake, S. D., et al. In Situ Characterization of Cu/CeO_2 Nanocatalysts for CO_2 Hydrogenation: Morphological Effects of Nanostructured Ceria on the Catalytic Activity. *J. Phys. Chem. C* **2018**, *122* (24), 12934–12943. DOI: 10.1021/acs.jpcc.8b03596.

(12) Ober, P.; Rogg, S.; Hess, C. Direct Evidence for Active Support Participation in Oxide Catalysis: Multiple Operando Spectroscopy of VO_x/Ceria. *ACS Catal.* **2020**, *10* (5), 2999–3008. DOI: 10.1021/acscatal.9b05174.

(13) Schumacher, L.; Weyel, J.; Hess, C. Unraveling the Active Vanadium Sites and Adsorbate Dynamics in VO_x/CeO_2 Oxidation Catalysts Using Transient IR Spectroscopy. *J. Am. Chem. Soc.* **2022**, *144* (32), 14874–14887. DOI: 10.1021/jacs.2c06303. Published Online: Aug. 2, 2022.

(14) Chen, J.; Zhu, J.; Zhan, Y.; Lin, X.; Cai, G.; Wei, K.; Zheng, Q. Characterization and catalytic performance of Cu/CeO_2 and Cu/MgO-CeO_2 catalysts for NO reduction by CO. *Appl. Catal. A: Gen.* **2009**, *363* (1-2), 208–215. DOI: 10.1016/j.apcata.2009.05.017.

(15) Salaev, M. A.; Salaeva, A. A.; Kharlamova, T. S.; Mamontov, G. V. Pt–CeO_2-based composites in environmental catalysis: A review. *Appl. Catal. B: Environ.* **2021**, *295*, 120286. DOI: 10.1016/j.apcatb.2021.120286.

(16) Zou, Z.-Q.; Meng, M.; Zha, Y.-Q. Surfactant-Assisted Synthesis, Characterizations, and Catalytic Oxidation Mechanisms of the Mesoporous MnO_x−CeO_2 and Pd/MnO_x−CeO_2 Catalysts Used for CO and C_3H_8 Oxidation. *J. Phys. Chem. C* **2010**, *114* (1), 468–477. DOI: 10.1021/jp908721a.

(17) Zhang, H.; Gao, X.; Gong, B.; Shao, S.; Tu, C.; Pan, J.; Wang, Y.; Dai, Q.; Guo, Y.; Wang, X. Catalytic combustion of CVOCs over MoO_x/CeO_2 catalysts. *Appl. Catal. B: Environ.* **2022**, *310*, 121240. DOI: 10.1016/j.apcatb.2022.121240.

(18) Schumacher, L.; Hess, C. The active role of the support in propane ODH over VO_x/CeO_2 catalysts studied using multiple operando spectroscopies. *J. Catal.* **2021**, *398*, 29–43. DOI: 10.1016/j.jcat.2021.04.006.

(19) Daniell, W.; Ponchel, A.; Kuba, S.; Anderle, F.; Weingand, T.; Gregory, D. H.; Knözinger, H. Characterization and Catalytic Behavior of VO_x-CeO_2 Catalysts for the Oxidative Dehydrogenation of Propane. *Top. Catal.* **2002**, *20* (1/4), 65–74. DOI: 10.1023/A:1016399315511.

(20) Giordano, F.; Trovarelli, A.; Leitenburg, C. de; Giona, M. A Model for the Temperature-Programmed Reduction of Low and High Surface Area Ceria. *J. Catal.* **2000**, *193* (2), 273–282. DOI: 10.1006/jcat.2000.2900.

(21) Guan, Y.; LI, C. Effect of CeO_2 Redox Behavior on the Catalytic Activity of a VO_x/CeO_2 Catalyst for Chlorobenzene Oxidation. *Chinese J. Catal.* **2007**, *28* (5), 392–394. DOI: 10.1016/S1872-2067(07)60033-3.

(22) Wu, Z.; Rondinone, A. J.; Ivanov, I. N.; Overbury, S. H. Structure of Vanadium Oxide Supported on Ceria by Multiwavelength Raman Spectroscopy. *J. Phys. Chem. C* **2011**, *115* (51), 25368–25378. DOI: 10.1021/jp2084605.

(23) Bruce, L. A.; Hoang, M.; Hughes, A. E.; Turney, T. W. Surface area control during the synthesis and reduction of high area ceria catalyst supports. *Appl. Catal. A: Gen.* **1996**, *134* (2), 351–362. DOI: 10.1016/0926-860X(95)00217-0.

(24) Iglesias-Juez, A.; Martínez-Huerta, M. V.; Rojas-García, E.; Jehng, J.-M.; Bañares, M. A. On the Nature of the Unusual Redox Cycle at the Vanadia Ceria Interface. *J. Phys. Chem. C* **2018**, *122* (2), 1197–1205. DOI: 10.1021/acs.jpcc.7b09832.

(25) Martínez-Huerta, M. V.; Coronado, J. M.; Fernández-García, M.; Iglesias-Juez, A.; Deo, G.; Fierro, J. L.G.; Banares, M. A. Nature of the vanadia-ceria interface in V^{5+}/CeO_2 catalysts and its relevance for the solid-state reaction toward $CeVO_4$ and catalytic properties. *J. Catal.* **2004**, *225* (1), 240–248. DOI: 10.1016/j.jcat.2004.04.005.

(26) Penschke, C.; Paier, J.; Sauer, J. Oligomeric Vanadium Oxide Species Supported on the CeO_2 (111) Surface: Structure and Reactivity Studied by Density Functional Theory. *J. Phys. Chem. C* **2013**, *117* (10), 5274–5285. DOI: 10.1021/jp400520j.

(27) Penschke, C.; Paier, J.; Sauer, J. Vanadium Oxide Oligomers and Ordered Monolayers Supported on CeO_2 (111): Structure and Stability Studied by Density Functional Theory. *J. Phys. Chem. C* **2018**, *122* (16), 9101–9110. DOI: 10.1021/acs.jpcc.8b01998.

(28) Wu, Z.; Kim, H.-S.; Stair, P. C.; Rugmini, S.; Jackson, S. D. On the structure of vanadium oxide supported on aluminas: UV and visible raman spectroscopy, UV-visible diffuse reflectance spectroscopy, and temperature-programmed reduction studies. *J. Phys. Chem. B* **2005**, *109* (7), 2793–2800. DOI: 10.1021/jp046011m.

(29) Klose, F.; Wolff, T.; Lorenz, H.; Seidelmorgenstern, A.; Suchorski, Y.; Piorkowska, M.; Weiss, H. Active species on γ-alumina-supported vanadia catalysts: Nature and reducibility. *J. Catal.* **2007**, *247* (2), 176–193. DOI: 10.1016/j.jcat.2007.01.013.

(30) Martínez-Huerta, M. V.; Deo, G.; Fierro, J. L. G.; Bañares, M. A. Changes in Ceria-Supported Vanadium Oxide Catalysts during the Oxidative Dehydrogenation of Ethane and Temperature-Programmed Treatments. *J. Phys. Chem. C* **2007**, *111* (50), 18708–18714. DOI: 10.1021/jp0772225.

(31) Suprun, W. Y.; Machold, T.; Papp, H. Comparison of a VO_x-TiO_2 and a VO_x/SbO_y-TiO_2 Industrial Catalyst in the Oxidative Scission of Methyl Ethyl Ketone and 2-Butanol to Acetic Acid. *Z. Phys. Chem.* **2008**, *222* (1), 129–151. DOI: 10.1524/zpch.2008.222.1.129.

(32) Waleska, P. S.; Hess, C. Oligomerization of Supported Vanadia: Structural Insight Using Surface-Science Models with Chemical Complexity. *J. Phys. Chem. C* **2016**, *120* (33), 18510–18519. DOI: 10.1021/acs.jpcc.6b01672.

(33) Briand, L. E.; Gambaro, L.; Thomas, H. Temperature-programmed reduction of V_2O_5 and coprecipitated V_2O_5−TiO_2 by hydrogen. *J. Therm. Anal.* **1995**, *44* (4), 803–821. DOI: 10.1007/BF02547266.

(34) Schilling, C.; Hess, C. Real-Time Observation of the Defect Dynamics in Working Au/CeO 2 Catalysts by Combined Operando Raman/UV–Vis Spectroscopy. *J. Phys. Chem. C* **2018**, *122* (5), 2909–2917. DOI: 10.1021/acs.jpcc.8b00027.

(35) Nottbohm, C. T.; Hess, C. Investigation of ceria by combined Raman, UV–vis and X-ray photoelectron spectroscopy. *Catal. Comm.* **2012**, *22*, 39–42. DOI: 10.1016/j.catcom.2012.02.009.

(36) Ziemba, M.; Schumacher, L.; Hess, C. Reduction Behavior of Cubic In_2O_3 Nanoparticles by Combined Multiple In Situ Spectroscopy and DFT. *J. Phys. Chem. Lett.* **2021**, *12* (15), 3749–3754. DOI: 10.1021/acs.jpclett.1c00892.

(37) Hess, C. Direct correlation of the dispersion and structure in vanadium oxide supported on silica SBA-15. *J. Catal.* **2007**, *248* (1), 120–123. DOI: 10.1016/j.jcat.2007.02.024.

(38) Laachir, A.; Perrichon, V.; Badri, A.; Lamotte, J.; Catherine, E.; Lavalley, J. C.; El Fallah, J.; Hilaire, L.; Le Normand, F.; Quéméré, E., et al. Reduction of CeO_2 by hydrogen. Magnetic susceptibility and Fourier-transform infrared, ultraviolet and X-ray photoelectron spectroscopy measurements. *J. Chem. Soc., Faraday Trans.* **1991**, *87* (10), 1601–1609. DOI: 10.1039/FT9918701601.

(39) Oelhafen, P. Practical surface analysis by auger and X-ray photoelectron spectroscopy. *J. Electron Spectrosc. Relat. Phenom.* **1984**, *34* (2), 203. DOI: 10.1016/0368-2048(84)80044-4.

(40) Suzuki, T.; Kosacki, I.; Anderson, H. U.; Colomban, P. Electrical Conductivity and Lattice Defects in Nanocrystalline Cerium Oxide Thin Films. *J. Am. Ceram. Soc.* **2001**, *84* (9), 2007–2014. DOI: 10.1111/j.1151-2916.2001.tb00950.x.

(41) Kainbayev, N.; Sriubas, M.; Virbukas, D.; Rutkuniene, Z.; Bockute, K.; Bolegenova, S.; Laukaitis, G. Raman Study of Nanocrystalline-Doped Ceria Oxide Thin Films. *Coatings* **2020**, *10* (5), 432. DOI: 10.3390/coatings10050432.

(42) Weber; Hass; McBride. Raman study of CeO_2: Second-order scattering, lattice dynamics, and particle-size effects. *Phys. Rev. B Condens. Matter* **1993**, *48* (1), 178–185. DOI: 10.1103/PhysRevB.48.178.

(43) Loridant, S. Raman spectroscopy as a powerful tool to characterize ceria-based catalysts. *Catal. Today* **2021**, *373*, 98–111. DOI: 10.1016/j.cattod.2020.03.044.

(44) Dohčević-Mitrović, Z. D.; Radović, M.; Šćepanović, M.; Grujić-Brojčin, M.; Popović, Z. V.; Matović, B.; Bošković, S. Temperature-dependent Raman study of $Ce_{0.75}Nd_{0.25}O_{2-\delta}$ nanocrystals. *Appl. Phys. Lett.* **2007**, *91* (20), 203118. DOI: 10.1063/1.2815928.

(45) Shvets, P.; Dikaya, O.; Maksimova, K.; Goikhman, A. A review of Raman spectroscopy of vanadium oxides. *J. Raman Spectrosc.* **2019**, *50* (8), 1226–1244. DOI: 10.1002/jrs.5616.

(46) Badri, A.; Binet, C.; Lavalley, J.-C. An FTIR study of surface ceria hydroxy groups during a redox process with H_2. *J. Chem. Soc., Faraday Trans.* **1996**, *92* (23), 4669. DOI: 10.1039/FT9969204669.

(47) Baron, M.; Abbott, H.; Bondarchuk, O.; Stacchiola, D.; Uhl, A.; Shaikhutdinov, S.; Freund, H.-J.; Popa, C.; Ganduglia-Pirovano, M. V.; Sauer, J. Resolving the Atomic Structure of Vanadia Monolayer Catalysts: Monomers, Trimers, and Oligomers on Ceria. *Angew. Chem. Int. Ed.* **2009**, *121* (43), 8150–8153. DOI: 10.1002/ange.200903085.

(48) Silversmit, G.; Depla, D.; Poelman, H.; Marin, G. B.; Gryse, R. de. Determination of the V2p XPS binding energies for different vanadium oxidation states (V^{5+} to V^{0+}). *J. Electron Spectrosc. Relat. Phenom.* **2004**, *135* (2-3), 167–175. DOI: 10.1016/j.elspec.2004.03.004.

(49) Eberhardt, M. A.; Proctor, A.; Houalla, M.; Hercules, D. M. Investigation of V Oxidation States in Reduced V/Al2O3Catalysts by XPS. *J. Catal.* **1996**, *160* (1), 27–34. DOI: 10.1006/jcat.1996.0120.

(50) Skorodumova, N. V.; Ahuja, R.; Simak, S. I.; Abrikosov, I. A.; Johansson, B.; Lundqvist, B. I. Electronic, bonding, and optical properties of CeO_2 and Ce_2O_3 from first principles. *Phys. Rev. B Condens. Matter* **2001**, *64* (11), 548. DOI: 10.1103/PhysRevB.64.115108.

(51) Binet, C.; Badri, A.; Lavalley, J.-C. A Spectroscopic Characterization of the Reduction of Ceria from Electronic Transitions of Intrinsic Point Defects. *J. Phys. Chem.* **1994**, *98* (25), 6392–6398. DOI: 10.1021/j100076a025.

(52) Castleton, C. W. M.; Kullgren, J.; Hermansson, K. Tuning LDA+U for electron localization and structure at oxygen vacancies in ceria. *J. Chem. Phys.* **2007**, *127* (24), 244704. DOI: 10.1063/1.2800015.

(53) Lamoureux, B.; Singh, V. R.; Jovic, V.; Kuyyalil, J.; Su, T.-Y.; Smith, K. E. Structural and electronic properties of thermally evaporated V_2O_5 epitaxial thin films. *Thin Solid Films* **2016**, *615*, 409–414. DOI: 10.1016/j.tsf.2016.07.062.

(54) Li, Z.; Werner, K.; Chen, L.; Jia, A.; Qian, K.; Zhong, J.-Q.; You, R.; Wu, L.; Zhang, L.; Pan, H., et al. Interaction of Hydrogen with Ceria: Hydroxylation, Reduction, and Hydride Formation on the Surface and in the Bulk. *Chemistry* **2021**, *27* (16), 5268–5276. DOI: 10.1002/chem.202005374. Published Online: Feb. 18, 2021.

(55) Höcker, J.; Krisponeit, J.-O.; Schmidt, T.; Falta, J.; Flege, J. I. The cubic-to-hexagonal phase transition of cerium oxide particles: dynamics and structure. *Nanoscale* **2017**, *9* (27), 9352–9358. DOI: 10.1039/c6nr09760j.

(56) Ma, R.; Jahurul Islam, M.; Amaranatha Reddy, D.; Kim, T. K. Transformation of CeO_2 into a mixed phase CeO_2/Ce_2O_3 nanohybrid by liquid phase pulsed laser ablation for enhanced photocatalytic activity through Z-scheme pattern. *Ceram. Int.* **2016**, *42* (16), 18495–18502. DOI: 10.1016/j.ceramint.2016.08.186.

(57) Körner, R.; Ricken, M.; Nölting, J.; Riess, I. Phase transformations in reduced ceria: Determination by thermal expansion measurements. *J. Solid State Chem.* **1989**, *78* (1), 136–147. DOI: 10.1016/0022-4596(89)90137-0.